

# Presupernova neutrinos: realistic emissivities from stellar evolution

Kelly M. Patton\* and Cecilia Lunardini†

*Department of Physics, Arizona State University, Tempe, AZ 85287-1504 USA*

(Dated: November 10, 2015)

We present a new calculation of neutrino emissivities and energy spectra from a presupernova, a massive star going through the advanced stages of nuclear burning in the months before becoming a supernova. The contributions from beta decay and electron capture, pair annihilation, plasmon decay, and the photoneutrino process are modeled in detail, using updated tabulated nuclear rates. We also use realistic conditions of temperature, density, electron fraction and nuclear isotopic composition of the star from the state of the art stellar evolution code MESA. It is found that beta processes contribute substantially to the neutrino flux above realistic detection thresholds of few MeV, at selected positions and times in the evolution of the star.

PACS numbers: 14.60.Lm, 97.60.-s

## I. INTRODUCTION

A very luminous burst of neutrinos is the first signal that we receive – possibly together with gravitational waves – informing us that a star’s core has collapsed, and that just a few hours afterwards the star will explode, becoming a supernova. Since their first (and only) detection in 1987 [1–3], neutrinos from stellar collapse have been studied in their rich phenomenology, including their role in the dynamics of collapse and explosion, the effects on the r-process nucleosynthesis, and the complicated pattern of neutrino flavor oscillations inside the star and in the Earth (see e.g. [4]).

Interestingly, neutrinos can also offer a unique signature of the stages of stellar evolution that lead up to collapse (“presupernova”), on which still little is known, at least observationally, compared to the dramatic post-collapse events. As a massive star ( $M \gtrsim 8M_\odot$ , with  $M_\odot$  the mass of the Sun) nears the end of its lifetime, the chain of nuclear burning in its core and inner shells proceeds through the fusion of progressively heavier elements. The central temperature and density of the star increase dramatically, resulting in an equally dramatic increase in the flux and average energies of neutrinos emitted. These neutrinos could become detectable months before the collapse, during the oxygen-burning phase, for the closest supernova candidate, Betelgeuse. Days or hours before (silicon-burning phase) might be more realistic for a star a few kiloparsecs away [5].

Although challenging, the observation of presupernova neutrinos would be extremely rewarding: it would offer an unprecedented direct probe of nuclear fusion beyond hydrogen and helium, and give us a first-hand narrative of the very late stages of stellar evolution in terms of density and temperature near the star’s core. Considering the excellent timing resolution of current neutrino detectors, this narrative could be seen in real time, and would be a precious alert of the upcoming post-collapse neutrino burst and supernova.

Besides their detection, the production and propagation of presupernova neutrinos are important ingredients of models of

stellar evolution. In the later stages of nuclear burning, neutrinos become the main source of energy loss while also increasing the entropy of the star as it nears core collapse [6]. The physics of these neutrinos is interesting also as an important application of the more general problem of neutrino emission in hot and dense stellar matter.

With these motivations, studies have been conducted on the neutrino emissivity of stars in the presupernova stage. The luminosities and spectra have been modeled, for generic typical presupernova parameters [5, 7, 8] and arguments of nuclear statistical equilibrium [9], or, more recently, using realistic profiles of temperature, density and chemical potential from numerical models of stellar evolution [10]. These studies focused mainly on neutrino production via pair annihilation and  $\beta$  processes; their results were used to assess the detectability of presupernova neutrinos, with encouraging results for the most massive detectors currently envisioned [5, 7, 8]. A dedicated study of the potential of the KamLAND experiment has appeared recently [11].

In this work we present an updated and more detailed calculation of the presupernova neutrinos emission. We model the neutrino emissivities and spectra by including all the four main neutrino production processes:  $\beta$  decay and electron capture, pair annihilation, plasmon decay, and the photoneutrino process. These processes are modeled using updated nuclear rate tables [12, 13] as a supplement to the classic ones by Fuller, Fowler and Newman [14–17]. The relevant microphysics is then applied to a realistic star using the detailed profiles of temperature, density, and nuclear isotopic composition from the state-of-the-art stellar evolution code MESA (Modules for Experiments in Stellar Astrophysics) [18–20]. We place emphasis on modeling of the neutrino spectrum above a realistic detection threshold of 2 MeV; this requires including certain  $\beta$  processes that are subdominant in the total energy budget of the star.

The paper is structured as follows. After a summary of background information (sec. II), the relevant formalism of neutrino emissivities and spectra is discussed in sec. II A for  $\beta$ -processes, and in sec. II B for thermal processes. In sec. III numerical results are shown for several steps of a star’s presupernova evolution, as modeled by MESA. A discussion and final considerations are given in sec. IV.

\*Electronic address: kelly.patton@asu.edu

†Electronic address: cecilia.lunardini@asu.edu

Processes		Formulae	Main References
Beta	$\beta^\pm$ decay	$A(N, Z) \rightarrow A(N-1, Z+1) + e^- + \nu_e$ $A(N, Z) \rightarrow A(N+1, Z-1) + e^+ + \bar{\nu}_e$	[9, 12–17]
	$e^+/e^-$ capture	$A(N, Z) + e^- \rightarrow A(N+1, Z-1) + \nu_e$ $A(N, Z) + e^+ \rightarrow A(N-1, Z+1) + \bar{\nu}_e$	
Thermal	plasma	$\gamma^* \rightarrow \nu_\alpha + \bar{\nu}_\alpha$	[21, 22]
	photoneutrino	$e^\pm + \gamma \rightarrow e^\pm + \nu_\alpha + \bar{\nu}_\alpha$	[23]
	pair	$e^+ + e^- \rightarrow \nu_\alpha + \bar{\nu}_\alpha$	[24]

TABLE I: Summary of the processes included in this work, with the main references to prior literature.

## II. NEUTRINO PRODUCTION IN A PRESUPERNOVA ENVIRONMENT

About  $\sim 10^3$  years before becoming a supernova, a star begins to experience the fusion of heavy (beyond helium) elements. First, carbon fusion is ignited; as the temperature and density increases, then the fusion of Ne, O, and Si take place in the core of the star. Each stage is faster than the previous one: the core O burning phase only lasts a few months, and the core Si burning only takes a few days [6]. Immediately before collapse, the star is characterized by a shell structure, with an iron core at the center, surrounded by shells where heavy element fusion is still taking place efficiently.

In the increasingly dense and hot environment of a presupernova, neutrinos are produced more and more abundantly through several processes, which we broadly categorize as  $\beta$  and thermal. Here the neutrino emissivities and spectra are calculated for the four main processes, using analytic and semi-analytic results from the literature, as summarized in Table I. Each process is discussed in detail in the subsections below.

### A. $\beta$ Processes

When a star reaches the presupernova phase, its nuclear isotopic composition is complex and constantly changing. Therefore, to calculate the  $\nu_e$  and  $\bar{\nu}_e$  fluxes from beta processes (Table I) requires information on a vast array of nuclear transitions.

Here we use the rate tables compiled by Fuller, Fowler and Newman (FFN) [14–17], Oda *et al.* (OEA) [13], and Langanke and Martinez-Pinedo (LMP) [12]. Each table uses shell model calculations, including experimental data when available, to find rates of electron (positron) capture and  $\beta^\pm$  decays for a grid of temperature and density values, under the assumption that there is a strong contribution from Gamow-Teller (GT) transitions. The FFN table covers isotopes with  $21 \leq A \leq 60$ , while OEA covers  $17 \leq A \leq 39$  and LMP is calculated for  $45 \leq A \leq 65$ . Where overlap between differ-

ent tables occurs, precedence is given, in order, to LMP, then OEA and finally FFN. This is the same convention used by MESA [18].

Let us summarize the calculation of neutrino  $\beta$  emissivities and spectra. The rate of weak decay from the  $i^{\text{th}}$  parent state to the  $j^{\text{th}}$  daughter state is written as [14]

$$\lambda_{ij} = \log 2 \frac{f_{ij}(T, \rho, \mu_e)}{\langle ft \rangle_{ij}}. \quad (1)$$

The quantity  $\langle ft \rangle_{ij}$  is the comparative half-life for the process, and is related to the weak interaction matrix element. For the tables of FFN, OEA, and LMP, the value of  $\langle ft \rangle$  is taken either from experimental measurements or from estimates of the strength of Gamow-Teller and Fermi transitions.

The function  $f_{ij}(T, \rho, \mu_e)$  is the phase space integral for the process. The phase space of an outgoing electron with momentum  $p'$  is given by

$$dn_{p'} = p'^2 dp' \left( 1 - \frac{1}{1 + \exp((E_{e'} - \mu_e)/kT)} \right), \quad (2)$$

while for an incoming electron with momentum  $p$  it is

$$dn_p = p^2 dp \left( \frac{1}{1 + \exp((E_e - \mu_e)/kT)} \right). \quad (3)$$

Here  $p$  and  $E_e = \sqrt{p^2 + m_e^2}$  are the momentum and energy of the electron,  $\mu_e$  is the chemical potential, and  $T$  is the temperature. As in [9], we define the chemical potential including the rest mass, so that  $\mu_{e^-} = -\mu_{e^+}$ . The outgoing neutrinos are assumed to have no inhibition of the final state [14], so the phase space factor is simply  $E_\nu^2 dE_\nu$ . In other words, while the incoming and outgoing electrons must conform to a Fermi-Dirac distribution, neutrinos have no such restriction.

For a given nuclear transition, the  $Q$ -value is defined as [14]

$$Q_{ij} = M_p - M_d + E_i - E_j, \quad (4)$$

where  $M_p$  and  $E_i$  ( $M_d$  and  $E_j$ ) are the mass and excitation energy of the parent (daughter) nucleus. Since we are interested in the rate as a function of neutrino energy, we can

rewrite the electron phase space integrals, Eqs. (2)-(3), in terms of the neutrino energy,  $E_\nu$ , using energy conservation, i.e.,  $Q_{ij} = E_e + E_\nu$  for beta decay, and  $Q_{ij} + E_e = E_\nu$  for electron capture. These phase space integrals contain all of the dependence on neutrino energy, and thus solely determine the neutrino energy spectra.

Following the approach of Langanke *et al.* [25], we adopt a single, effective  $Q$ -value,  $Q$ , for each isotope, and treat it as a fit parameter. This effective  $Q$ -value is found by requiring that the average neutrino energy matches the value obtained from the nuclear rate tables, i.e.:

$$\langle E_{\nu,\bar{\nu}} \rangle = \frac{\int_0^\infty \left( \frac{d\lambda}{dE_\nu} \right) E_\nu dE_\nu}{\int_0^\infty \left( \frac{d\lambda}{dE_\nu} \right) dE_\nu} = \frac{\mathcal{E}^{\nu,\bar{\nu}}}{\lambda^{EC,PC} + \lambda^{\beta^\pm}}, \quad (5)$$

where the quantities on the right side of the equation are obtained from the rate tables. Here  $\lambda^{EC,PC}$  and  $\lambda^{\beta^\pm}$  are the electron (positron) capture rate and  $\beta^\pm$  decay rates [12];  $\lambda = \lambda^{EC,PC} + \lambda^{\beta^\pm}$ , and  $\mathcal{E}^{\nu,\bar{\nu}}$  is the rate of energy loss as (anti-) neutrinos. Here and throughout the paper, subscripts such as in  $\langle E_{\nu,\bar{\nu}} \rangle$  indicate that an equation is true for, in this example,  $\langle E_\nu \rangle$  and  $\langle E_{\bar{\nu}} \rangle$  with all subscripted values in the equation taking either  $\nu$  or  $\bar{\nu}$  as necessary.

Note that  $\langle E_{\nu,\bar{\nu}} \rangle$  is a combined value, including both the capture and decay values weighted by the respective rates. Therefore, by construction, the  $Q$ -value found from Eq. (5) is the same for both decay and capture.

Combining Eqs. (1)-(5), we find the spectra for the weak processes for a single isotope:

$$\phi_{EC,PC} = N_{EC,PC} \frac{E_\nu^2 (E_\nu - Q)^2}{1 + \exp((E_\nu - Q - \mu_e)/kT)} \times \Theta(E_\nu - Q - m_e) \quad (6)$$

$$\phi_\beta = N_\beta \frac{E_\nu^2 (Q - E_\nu)^2}{1 + \exp((E_\nu - Q + \mu_e)/kT)} \times \Theta(Q - m_e - E_\nu), \quad (7)$$

where  $N_i$  is a normalization factor defined such that

$$\lambda^i = \int_0^\infty \phi_i dE_\nu \quad i = EC, PC, \beta^\pm. \quad (8)$$

Let us note that the presupernova environment is different from that of a supernova: for a supernova the high electron degeneracy inhibits beta decay, so that electron capture plays a stronger role [25, 26]; in our case of interest, instead, lower degeneracies allow  $\beta$  decays to proceed. Their importance has been emphasized in [27–30].

Finally, the total  $\nu_e$  (or  $\bar{\nu}_e$ ) spectrum is found by a weighted sum over all the isotopes present:

$$\Phi_{\nu,\bar{\nu}} = \sum_k X_k \phi_k \frac{\rho}{m_p A_k}, \quad (9)$$

where  $X_k$  is the abundance of isotope  $k$ ,  $\phi_k$  is the sum of the normalized electron (positron) capture and  $\beta^\pm$  decay spectra for isotope  $k$ ,  $\rho$  is the density of the star,  $m_p$  is the mass of the proton, and  $A_k$  is the atomic number of isotope  $k$  [9]. The values of  $X_k$  and  $\rho$  are taken from MESA calculations [18–20].

The features of the spectrum  $\Phi_{\nu,\bar{\nu}}$  depend on the temperature, density, and isotopic abundances. For the center of a star immediately before collapse ( $T \approx 4 - 5 \times 10^9$  K,  $\rho \approx 10^7$  g/cm<sup>3</sup>), the total spectrum can extend to several MeV.

## B. Thermal Processes

Let us now discuss the three most important thermal processes: plasmon decay, photoneutrino production, and pair annihilation (Table I). The total emissivities of all these processes, over a range of temperatures and densities, were discussed in detail by Itoh *et al.* [31–35]. The differential rates and emissivities of selected process have been discussed by several authors [10, 11, 21–24]. In this section, we summarize the formalism relevant to our calculation.

### 1. Plasma Neutrino Process

In the plasma neutrino process, an excitation in the plasma (plasmon) decays into a neutrino-antineutrino pair. As shown in ref. [35], plasma neutrinos dominate the total emissivity at high densities. Detailed derivations and discussions of this process are given in refs. [21, 22]. Drawing from this literature, here the essential equations for calculating the plasmon decay neutrino spectrum are summarized. Additional equations and definitions are given in Appendix A.

The total rate and emissivity are given by the integrals [21]

$$R = \sum_\epsilon \int \frac{d^3k}{2\omega(2\pi)^3} Z(k) \frac{d^3q_1}{2\mathcal{E}_1(2\pi)^3} \frac{d^3q_2}{2\mathcal{E}_2(2\pi)^3} \langle |\mathcal{M}|^2 \rangle_{f_{\gamma^*}}(\omega)(2\pi)^4 \delta^4(K - Q_1 - Q_2) \quad (10)$$

$$Q = \sum_\epsilon \int \frac{d^3k}{2\omega(2\pi)^3} Z(k) \frac{d^3q_1}{2\mathcal{E}_1(2\pi)^3} \frac{d^3q_2}{2\mathcal{E}_2(2\pi)^3} (\mathcal{E}_1 + \mathcal{E}_2) \langle |\mathcal{M}|^2 \rangle_{f_{\gamma^*}}(\omega)(2\pi)^4 \delta^4(K - Q_1 - Q_2), \quad (11)$$

where  $Q_{1,2} = (\mathcal{E}_{1,2}, \mathbf{q}_{1,2})$  are the four-momenta of the daughter neutrino pair;  $K = (\omega, \mathbf{k})$  and  $f_{\gamma^*}$  are the plasmon four-momentum and spectrum:

$$f_{\gamma^*} = \frac{1}{e^{\omega_{T,L}/kT} - 1}. \quad (12)$$

The factor  $Z(k)$  in Eqs. (10) and (11) is the residue from integrating around the pole in the propagator; see Appendix A for an approximate form of it. The sums in Eqs. (10) and (11) are over the polarizations appropriate for the decay mode. There are two possible decay modes: transverse (T), which has two polarizations, and longitudinal (L), with one polarization.

The term  $\langle |\mathcal{M}|^2 \rangle$  is the squared matrix element for the process. The effective vertex for plasmon decay has both vector and axial vector pieces [36]. For the longitudinal decay mode, the axial vector term disappears, leaving the squared matrix

element as [21]:

$$\langle |\mathcal{M}|^2 \rangle_L = 2 \frac{G_F^2 (C_V^f)^2}{\pi \alpha} \left( \frac{\omega_L^2 - k^2}{k^2} \right)^2 \Pi_L^2(\omega_L, k) \times \left[ \frac{(\mathcal{E}_1 \omega_L - \mathbf{q}_2 \cdot \mathbf{k})(\mathcal{E}_2 \omega_L - \mathbf{q}_2 \cdot \mathbf{k})}{\omega_L^2 - k^2} + \frac{(\mathbf{k} \cdot \mathbf{q}_1)(\mathbf{k} \cdot \mathbf{q}_2)}{k^2} - \frac{\mathcal{E}_1 \mathcal{E}_2 + \mathbf{q}_1 \cdot \mathbf{q}_2}{2} \right]. \quad (13)$$

On the other hand, both vector and axial vector pieces survive in the calculation of the transverse decay mode. After squaring, we are left with a transverse vector term proportional to  $(C_V^f)^2$ , an axial term with coefficient  $(C_A^f)^2$ , and a mixed term with a factor  $(C_A^f C_V^f)$  [21]. Put together, the squared matrix element for the transverse decay mode is

$$\langle |\mathcal{M}|^2 \rangle_T = \frac{G_F^2}{\pi \alpha} \left[ ((C_V^f)^2 \Pi_T^2(\omega_T, k) + (C_A^f)^2 \Pi_A^2(\omega_T, k)) \times \left( \mathcal{E}_1 \mathcal{E}_2 - \frac{(\mathbf{k} \cdot \mathbf{q}_1)(\mathbf{k} \cdot \mathbf{q}_2)}{2} \right) + 2(C_A^f C_V^f) \frac{\Pi_A(\omega_T, k) \Pi_T(\omega_T, k)}{k} \times (\mathcal{E}_1(\mathbf{k} \cdot \mathbf{q}_2) - \mathcal{E}_2(\mathbf{k} \cdot \mathbf{q}_1)) \right]. \quad (14)$$

The functions  $\Pi_{L,T,A}$  are the longitudinal, transverse, and axial polarization functions (Appendix A). The total emissivity for the plasmon decay process is found by summing all of these channels. The vector and axial couplings,  $C_V^f$  and  $C_A^f$ , are

$$C_V^e = \frac{1}{2} + 2 \sin^2(\theta_W) \quad C_A^e = \frac{1}{2} \quad (15)$$

$$C_V^x = C_V^e - 1 \quad C_A^x = C_A^e - 1, \quad (16)$$

with  $\sin^2(\theta_W) = 0.226$ . The difference in these couplings results in a suppression of the  $\nu_x$  flavors by factors of  $(C_V^x/C_V^e)^2 \approx 3 \times 10^{-3}$  [22].

After integrating Eqs. (10) and (11) over the plasmon momentum and the angle between the outgoing neutrinos, one gets the rate, differential in the neutrino energy  $\mathcal{E}_1$  [22]:

$$\frac{dR_{L,T}}{d\mathcal{E}_1} = \int_0^\infty d\mathcal{E}_2 \frac{g_{L,T}}{\pi^4} Z_{L,T} \langle |\mathcal{M}|^2 \rangle_{L,T} f_\gamma J_{L,T} S, \quad (17)$$

with  $g_T = 2$  and  $g_L = 1$  accounting for the number of polarizations for each mode. The new factor  $J_{L,T}$  is the Jacobean resulting from the  $\delta$  function integration. The factor  $S$ , is a product of step functions, describing the physically relevant region:

$$S = \Theta(4\mathcal{E}_1 \mathcal{E}_2 - m_{L,T}^2) \Theta(\mathcal{E}_1 + \mathcal{E}_2 - \omega_{L,T}) \Theta(\omega_{max} - \mathcal{E}_1 - \mathcal{E}_2). \quad (18)$$

The maximum plasmon energy,  $\omega_{max}$ , is finite for longitudinal plasmons, and depends on the temperature and density of the environment. Instead,  $\omega_{max} \rightarrow \infty$  for transverse plasmons. We have used the Braaten-Segel approximations [36] in all of these calculations, allowing the differential rate to be calculated analytically. The expressions for various plasma

parameters,  $\omega_{max}$ ,  $Z_{L,T}$ , and  $J_{L,T}$  in this approximation are given in Appendix A. The total emissivity calculated through this method is consistent with the Itoh *et al.* formula for the plasma process.

The spectra of neutrinos from plasmon decay are typically colder than those from other processes (see figs. 3 and 4). The neutrinos resulting from longitudinal plasmon decay are limited by  $\omega_{max}$ , with  $\omega_{max} < \text{MeV}$  for typical presupernova temperatures and densities. Neutrinos from transverse plasmon decay have no such energy restriction, however, and can extend beyond 1 MeV in some cases. Probably, the plasmon decay contribution can not be individually identified in a detector; nevertheless it can have a major impact on the total neutrino emissivity at some points in the lifetime of the star.

## 2. Photoneutrino Process

For the photoneutrino process, we follow the extensive discussion in Dutta *et al.* [23]. The calculation of rates and emissivities is very similar to that for the plasma neutrino process. In this case, the total rate and emissivity are calculated by performing the integrals

$$R = \int \frac{2d^3p}{(2\pi)^3} \frac{f_e(E_P)}{2E_P} \int \frac{\xi d^3k}{(2\pi)^3} \frac{f_\gamma(\omega)}{2\omega} \times \int \frac{d^3p'}{(2\pi)^3} \frac{1 - f_e(E_{P'})}{2E_{P'}} \int \frac{d^3q_1}{(2\pi)^3} \frac{1}{2\mathcal{E}_1} \times \int \frac{d^3q_2}{(2\pi)^3} \frac{1}{2\mathcal{E}_2} (2\pi)^4 \delta^4(P + K - P' - Q_1 - Q_2) \times \frac{1}{\zeta} \sum_{s,\epsilon} |\mathcal{M}|^2 \quad (19)$$

$$Q = \int \frac{2d^3p}{(2\pi)^3} \frac{f_e(E_P)}{2E_P} \int \frac{\xi d^3k}{(2\pi)^3} \frac{f_\gamma(\omega)}{2\omega} \times \int \frac{d^3p'}{(2\pi)^3} \frac{1 - f_e(E_{P'})}{2E_{P'}} \int \frac{d^3q_1}{(2\pi)^3} \frac{1}{2\mathcal{E}_1} \times \int \frac{d^3q_2}{(2\pi)^3} \frac{1}{2\mathcal{E}_2} (2\pi)^4 \delta^4(P + K - P' - Q_1 - Q_2) \times (\mathcal{E}_1 + \mathcal{E}_2) \frac{1}{\zeta} \sum_{s,\epsilon} |\mathcal{M}|^2. \quad (20)$$

As in Eqs. (10) and (11), these expressions are integrals of the squared matrix element over the incoming and outgoing momenta, taking into account the photon and electron distributions and energy conservation. Here,  $P = (E_P, \mathbf{p})$  is the four momentum for the incoming electron and  $P' = (E_{P'}, \mathbf{p}')$  is the same for the outgoing electron. Following the notation defined in the plasma neutrino discussion,  $Q_{1,2} = (\mathcal{E}_{1,2}, \mathbf{q}_{1,2})$  are the four momenta for the outgoing neutrino pair and  $K = (\omega, \mathbf{k})$  is the four momentum of the photon.

The sums run over the polarization of the photon and spin of the incoming and outgoing electrons. Here the initial factor of 2 accounts for the spin of the incoming electron,  $\xi$  is due to the polarization of the incoming photon, and  $\zeta$  from the spins of the outgoing electron and neutrinos. Similar to



plasmon decay, there are transverse and longitudinal modes for the photoneutrino process. For the transverse mode of the photon,  $\xi = 2$  and  $\zeta = 4$ . In the longitudinal case,  $\xi = 1$  and  $\zeta = 2$ . [23].

As discussed in [23], the squared matrix element can be derived to be

$$\sum_{s,\epsilon} |\mathcal{M}^{T(L)}|^2 = 32e^2 G_F^2 \left[ ((C_V^f)^2 - (C_A^f)^2) m_e^2 \mathcal{M}_-^{T(L)} + ((C_V^f)^2 + (C_A^f)^2) \mathcal{M}_+^{T(L)} + C_V^f C_A^f \mathcal{M}_\times^{T(L)} \right] \quad (21)$$

For brevity, the expressions for  $\mathcal{M}_-$ ,  $\mathcal{M}_+$ , and  $\mathcal{M}_\times$  are given in Appendix B. The subscripts +, -, and  $\times$  refer to the combinations of  $C_V$  and  $C_A$ , which are subtracted, added, and multiplied, respectively.

The delta function in Eqs. (19) and (20) can be used to complete the integration over the incoming electron momentum  $\mathbf{p}$  and the incoming photon angle  $\theta_k$ . This allows us to define the angle  $\theta_k$  in terms of other variables as

$$\cos \theta_k = \frac{m_e^2 - M^2 - m_k^2 + 2E\omega}{2|\mathbf{p}_{\text{tot}}||\mathbf{k}|}, \quad (22)$$

where  $P_{\text{tot}} = P + K = P' + Q_1 + Q_2$  is the total four-momentum and  $P_{\text{tot}}^2 = M^2$ , with  $M^2$  defined as the invariant mass squared. This mass is the same for a given set of incoming and outgoing particles, but will change as the integration covers the possible phase space. Here  $K^2 = m_k^2 = \omega^2 - |\mathbf{k}|^2$  is the effective photon mass. Requiring that  $|\cos \theta_k| \leq 1$  gives the relevant ranges for the integration over  $\mathbf{k}$  for both the transverse and longitudinal modes (Appendix B).

As in ref. [23], here the coordinate system is such that one neutrino momentum is aligned with the z-axis, with the second neutrino momentum in the x-z plane at an angle  $\theta_{q_1, q_2}$ , while the outgoing electron momentum  $\mathbf{p}'$  is in an arbitrary direction defined by angles  $\theta_e$  and  $\phi_e$ . In this formalism, we can find the total four-momentum of the system  $P$ , and thus determine the momenta of the incoming photon and electron.

The result for the differential rates and emissivities is the following:

$$\begin{aligned} \frac{dR}{d\mathcal{E}_1} &= \frac{\pi^2}{(2\pi)^9} \mathcal{E}_1 \int_0^\infty \mathcal{E}_2 d\mathcal{E}_2 \int_{-1}^1 d\cos \theta_{q_1, q_2} \\ &\times \int_0^\infty \frac{|\mathbf{p}'|^2}{E_{p'}} d|\mathbf{p}'| \int_{-1}^1 d\cos \theta_e \\ &\times \int_0^{2\pi} d\phi_e [1 - f_e(E_{p'})] I(p', q_1, q_2) \end{aligned} \quad (23)$$

$$\begin{aligned} \frac{dQ}{d\mathcal{E}_1} &= \frac{\pi^2}{(2\pi)^9} \mathcal{E}_1 \int_0^\infty \mathcal{E}_2 d\mathcal{E}_2 \int_{-1}^1 d\cos \theta_{q_1, q_2} \\ &\times \int_0^\infty \frac{|\mathbf{p}'|^2}{E_{p'}} d|\mathbf{p}'| \int_{-1}^1 d\cos \theta_e \\ &\times \int_0^{2\pi} d\phi_e [1 - f_e(E_{p'})] \\ &(\mathcal{E}_1 + \mathcal{E}_2) I(p', q_1, q_2). \end{aligned} \quad (24)$$

where the integral  $I(p', q_1, q_2)$  is defined as

$$\begin{aligned} I(p', q_1, q_2) &= \frac{1}{2\pi^2} \int_0^\infty \frac{|\mathbf{k}|}{\omega} d|\mathbf{k}| \int_0^{2\pi} d\phi_k \\ &\times f_\gamma(\omega) f_e(E_p) \frac{1}{|\mathbf{p}|} \sum_{s,\epsilon} |\mathcal{M}^{T(L)}|^2. \end{aligned} \quad (25)$$

The seven-dimensional integrals in Eqs. (23)-(24) are calculated by a Monte Carlo method, as in [23]. As with the plasma process, our calculation using the methods of Dutta *et al.* [23] are consistent with the formula from Itoh *et al.* [34].

As will be shown in Section III, photoneutrinos dominate the total emissivity at a few locations in the outer shells of the star, in agreement with the results in [34]. However, for the part of the presupernova neutrino flux that is of most interest for detection – corresponding to higher temperatures and densities – these neutrinos are typically overwhelmed by pair and  $\beta$  process neutrinos.

### 3. Pair Annihilation Neutrinos

The emissivity for neutrinos from pair annihilation,  $e^+ + e^- \rightarrow \nu + \bar{\nu}$ , can be calculated similarly to Eqs. (10) and (11): the squared matrix element for this process has to be integrated over the incoming and outgoing momenta, including considerations for the electron and positron momentum distributions and energy conservation. The squared matrix element is

$$\begin{aligned} \mathcal{M}^2 &= 8G_F^2 \left( (C_A^f - C_V^f)^2 (P_1 \cdot Q_1) (P_2 \cdot Q_2) \right. \\ &\quad + (C_A^f + C_V^f)^2 (P_2 \cdot Q_1) (P_1 \cdot Q_2) \\ &\quad \left. + m_e^2 (C_V^2 - C_A^2) (Q_1 \cdot Q_1) \right), \end{aligned} \quad (26)$$

where  $P_{1,2} = (E_{1,2}, \mathbf{p}_{1,2})$  are the four-momenta of the incoming electron and positron, and  $Q_{1,2} = (E_{1,2}, \mathbf{q}_{1,2})$  are the four-momenta of the outgoing neutrino and antineutrino.

Following [24], first the integration over the electron and positron momenta and angles can be performed, so that the differential cross section is obtained:

$$d\sigma v = \frac{1}{2E_1} \frac{1}{2E_2} \frac{1}{(2\pi)^2} \delta^4(P_1 + P_2 - Q_1 - Q_2) \frac{d^3 q_1}{2E_1} \frac{d^3 q_2}{2E_2} M^2, \quad (27)$$

with  $v$  being the relative velocity of the electron-positron pair.

After some lengthy algebra (see the example in [37]), the differential cross section can be expressed in the form:

$$\begin{aligned} \frac{d\sigma v}{d\mathcal{E}_{1,2}} &= \frac{G_F^2}{8\pi E_1 E_2} \left[ (C_V^f + C_A^f)^2 H_{1,2} + (C_V^f - C_A^f)^2 H_{2,1} \right. \\ &\quad \left. + 2m_e^2 (C_V^2 - C_A^2) H_3 \right] \Theta, \end{aligned} \quad (28)$$

with  $\mathcal{E}_1$  corresponding to the neutrino and  $\mathcal{E}_2$  to the antineutrino. Note that this results in a slightly different spectrum for  $\nu_e$  than for  $\bar{\nu}_e$ . The step function  $\Theta$  in Eq. (28) is

$$\Theta = \begin{cases} 0 & \text{for } \mathcal{E}_i < \mathcal{E}_- \\ 1 & \text{for } \mathcal{E}_- < \mathcal{E}_i < \mathcal{E}_+ \\ 0 & \text{for } \mathcal{E}_i > \mathcal{E}_+ \end{cases} \quad i = 1, 2. \quad (29)$$

The minimum and maximum neutrino energies  $\mathcal{E}_\pm$ , defined in terms of the momentum and energy of the electron and positron, are

$$\mathcal{E}_\pm = \frac{1}{2}(E_1 + E_2) \pm \frac{1}{2}|\mathbf{p}_1 + \mathbf{p}_2| \quad (30)$$

The quantities  $H_k$  in Eq. (28) are written compactly as [24]

$$H_k = \sum_{j=1}^5 h_k^j |\mathbf{p}_1 + \mathbf{p}_2|^{-j}, \quad (31)$$

with the coefficients defined as:

$$h_1^1 = 2(\Delta - \mathcal{E}_i E_2)^2 \quad (32)$$

$$h_1^3 = -4\delta(\Delta - \mathcal{E}_i E_2)\Delta - p_1^2 \Delta^2 + \mathcal{E}_i p_1^2 p_2^2 \sin^2 \theta \quad (33)$$

$$h_1^5 = 3\delta^2 \Delta^2 \quad (34)$$

$$h_2^1 = 2E_1^2 \mathcal{E}_i^2 \quad (35)$$

$$h_2^3 = -4\mathcal{E}_i E_1 \delta \Delta - p_1^2 \Delta^2 + \mathcal{E}_i p_1^2 p_2^2 \sin^2 \theta \quad (36)$$

$$h_2^5 = 3\delta^2 \Delta^2 \quad (37)$$

$$h_3^1 = \Delta - \mathcal{E}_i(E_1 + E_2) \quad (38)$$

and

$$\delta = p_1(p_1 + p_2 \cos \theta) \quad (39)$$

$$\Delta = \mathcal{E}_i(E_1 + E_2) - P_1 \cdot P_2 - me^2 \quad (40)$$

The differential rate is then found by integrating over the incoming electron and positron momenta and distributions:

$$\frac{dR}{d\mathcal{E}_i} = \int d^3\mathbf{p}_1 d^3\mathbf{p}_2 \frac{d\sigma v}{d\mathcal{E}_i} f_1 f_2 \quad (41)$$

This final form is actually a three dimensional integral, over the magnitudes of  $\mathbf{p}_1$  and  $\mathbf{p}_2$  as well as the angle between them. We have performed this calculation using Monte Carlo integration.

In agreement with the results of Itoh *et al.* [34], the results of MESA show (Section III) that pair neutrinos are the major contributors to the neutrino flux from the center of the star where temperatures and densities are highest. The energies of these neutrinos can reach up to several MeV and, along with the  $\beta$  process, produce most of the potentially detectable neutrinos.

### III. RESULTS: NEUTRINO EMISSION IN AN EVOLVING STAR

In this section the formalism in sec. II is applied to a realistic presupernova simulation. Specifically, we use the stellar evolution code MESA (version r7624) [18–20] to obtain a detailed and consistent description of temperature, mass density, proton fraction, electron degeneracy, and isotopic composition inside the star, as functions of both time and radial coordinate.

For definiteness, we refer to the MESA output for a  $25 M_\odot$  star with solar metallicity (i.e., mass fraction  $Z = 0.02$  of elements heavier than He) and the nuclear network mesa\_201.net, which includes isotopes up to  $^{66}\text{Zn}$ . The code was set to run until the infall velocity near the edge of the Fe core exceeds  $V_{\max} = 1 \times 10^8 \text{ cm s}^{-1}$ , indicating that the core collapse has begun. This final instant is defined as  $t = 0$ , and all the earlier times  $t$  ( $t < 0$ ) will be defined relative to it, so that  $-t > 0$  will indicate the time-to-collapse.

For each time step of the evolution, MESA, using formulae from Itoh *et al.* [31–35], provides the energy emissivity  $Q$  (i.e., the total energy emitted per unit volume per unit time) for each production channel in Table I, as a function of the radial coordinate. Our calculated neutrino spectra are normalized to reproduce these emissivities. Using the spectra, we have calculated partial emissivities,  $Q_{th}$ , defined as the energy emitted in neutrinos having energy above a certain energy threshold  $E_{th}$ . To emphasize the part of the neutrino flux that is potentially detectable, below we discuss results for both  $Q$  and  $Q_{th}$ , as well as  $\nu_e$  and  $\bar{\nu}_e$  spectra, with  $E_{th} = 2 \text{ MeV}$  as an indicative threshold for detectability. This is a realistic value for liquid scintillator detectors (e.g., [38]); the threshold is typically higher than  $\sim 5 \text{ MeV}$  at liquid argon and water Cherenkov experiments [39, 40].

#### A. A neutrino history: emissivity profiles

Let us first trace the time evolution of a presupernova in terms of neutrino emission. We focus on the electron neutrino species, and do not include neutrino flavor oscillations. The  $\mu$  and  $\tau$  flavors (collectively denoted  $\nu_x$  here) only give subdominant contributions to rates and emissivities, because they are not produced in  $\beta$  processes, and are suppressed in thermal processes.

Results were generated with MESA for five times before collapse:  $t_1 = -107.2$  days,  $t_2 = -1.18$  day,  $t_3 = -12.01$  hrs,  $t_4 = -5.95$  hrs,  $t_5 = -0.99$  hr. At  $t_1$ , the star's core is in the O-burning phase;  $t_2$  through  $t_4$  are during the core Si-burning phase. At  $t_5$ , Si burning is occurring in an outer shell, around  $\log(R/R_\odot) \approx -2.5$ .

Fig. 1 shows the radial distribution of  $Q$  and  $Q_{th}$ , at each time step. At all times,  $Q$  is maximum in the region  $R \lesssim 10^{-2.5} R_\odot$ , and declines roughly as  $R^{-6}$  for larger radii.  $Q_{th}$  is within an order of magnitude or so of  $Q$  in the central region, and falls more steeply than  $Q$  with increasing radius. We note sharp, time-dependent discontinuities in these emissivities, which reflect the shell structure of the star.

Fig. 2 shows the temperature-density profiles, i.e., the temperature as a function of the density (multiplied by the electron fraction  $Y_e$ ), of the star at the times  $t_n$ . The dashings/colors in the curves indicate which process contributes most strongly to the total and partial emissivities,  $Q$  and  $Q_{th}$ . As expected from prior literature [34], generally  $Q$  is mostly due to  $\beta$  processes at lower density, whereas pair production dominates for  $\rho Y_e \gtrsim 10^6 \text{ g cm}^{-3}$ . Small islands of photoneutrino preponderance are observed at  $\rho Y_e \sim 10^4 \text{ g cm}^{-3}$ . The same general trend is observed for  $Q_{th}$ , with the major differ-

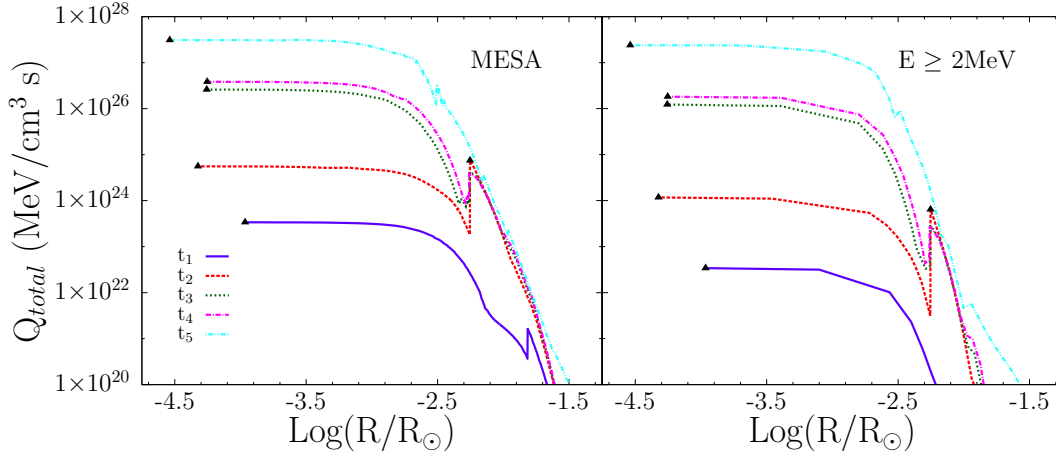


FIG. 1: *Left*: The total neutrino emissivity in the star, as a function of the radial coordinate, calculated by MESA for the times  $(t_1, t_2, t_3, t_4, t_5) = (-10^2 \text{ d}, -1 \text{ d}, -12 \text{ hr}, -6 \text{ hr}, -1 \text{ hr})$ . *Right*: The emissivity for neutrinos with energy  $E > 2 \text{ MeV}$ . In both figures, sample points are marked; details about them are given in Table II and Figs. 3 and 4.

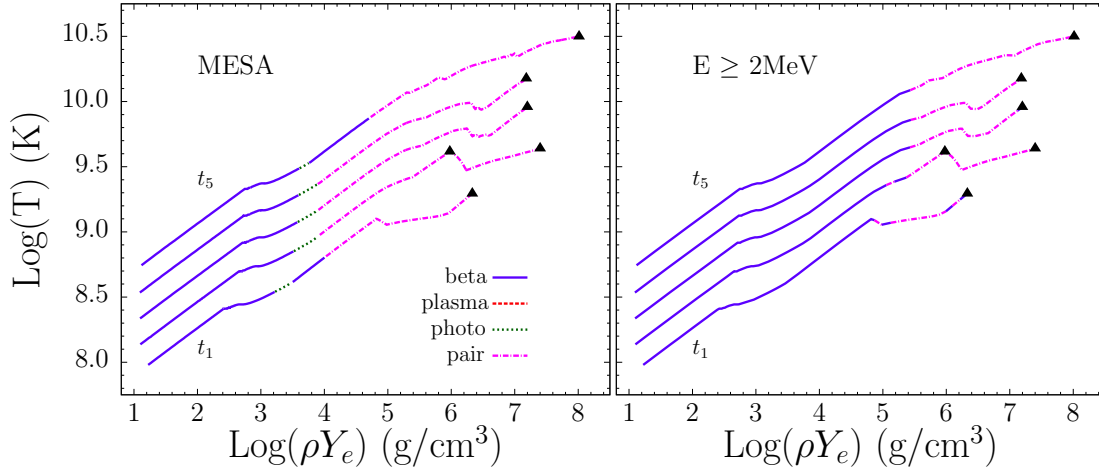


FIG. 2: *Left*: Origin of the dominant neutrino emissivity as calculated by MESA as a function of both temperature and density, for the same time instants  $t_n$  as in fig. 1 ( $n = 1, 5$ , from bottom to top). Each curve describes the temperature and density encountered at different radii within the star at a given time  $t$ . The different dashings/colors indicate which process dominates the total emissivity (see legend). For better visibility, the curve for the time  $t_n$  is shifted upwards vertically by  $0.2(n - 1)$  units. The selected points in Table II are marked. *Right*: the same figure, but for the emissivity of potentially detectable neutrinos (with energy  $E \geq 2 \text{ MeV}$ ).

ence that  $\beta$  dominance is much more extended to high density, and islands of  $\beta$ -dominated emissivity are seen for  $\rho Y_e$  as high as  $\rho Y_e \sim 10^7 \text{ g cm}^{-3}$ . This suggests the importance of  $\beta$  processes for the detectable part of the neutrino spectrum, which is investigated in the next section.

## B. Spectra

We now illustrate the  $\nu_e$  and  $\bar{\nu}_e$  energy spectra for selected points inside the star at the times  $t_n$ . The details about them are given in Table II. These points represent examples of cases when  $\beta$  processes contribute substantially to the neutrino spectrum in the detectable energy window. All points, except for point (s2), are at the center of the stellar core. Point (s2) is situated at the edge of the core at time  $t_2$ , the beginning of core

point	$\log(T/K)$	$\log(\rho/g\text{ cm}^{-3})$	$Y_e$	$\log(R/R_\odot)$	$t$	$\log(Q/\text{MeV cm}^{-3}\text{ s}^{-1})$	$\log(Q_{th}/\text{MeV cm}^{-3}\text{ s}^{-1})$
(c1)	9.294	6.6350	0.498	-3.965	$t_1 = -107.2$ days	$3.380 \times 10^{23}$	$3.408 \times 10^{22}$
(c2)	9.440	7.7102	0.490	-4.323	$t_2 = -1.18$ day	$5.564 \times 10^{24}$	$1.178 \times 10^{24}$
(s2)	9.416	6.280	0.498	-2.253	$t_2 = -1.18$ day	$7.468 \times 10^{24}$	$6.433 \times 10^{23}$
(c3)	9.558	7.511	0.488	-4.257	$t_3 = -12.01$ hrs	$2.596 \times 10^{26}$	$1.225 \times 10^{26}$
(c4)	9.577	7.500	0.482	-4.253	$t_4 = -5.95$ hrs	$3.830 \times 10^{26}$	$1.820 \times 10^{26}$
(c5)	9.699	8.356	0.455	-4.539	$t_5 = -0.99$ hr	$3.086 \times 10^{27}$	$2.391 \times 10^{27}$

TABLE II: Selected points in the evolution of the star. The columns give the time (with  $t = 0$  the time of collapse, see text), radial coordinate, temperature, density times electron fraction, and neutrino emissivity (total of all flavors). Points labeled (c1) - (c5) are at the stellar core, while point (s2) is in an outer shell.

silicon burning.

Figs. 3 and 4 show the contribution of the different processes to the neutrino spectra. We see that pair production has the dominant contribution at  $E \sim \text{MeV}$ , with plasma neutrinos and photoneutrinos becoming increasingly important, or even dominant, at lower energies. In the tail of the spectrum,  $E \gtrsim E_{th} = 2 \text{ MeV}$ , the major contributions to the energy spectrum are from pair production and  $\beta$  processes. The latter can dominate by several orders of magnitude at  $E \sim 7 - 10 \text{ MeV}$ , which is a realistic energy threshold for a Mt-mass water Cherenkov detector [40]. Generally,  $\beta$  processes contribute more strongly to the  $\nu_e$  spectrum, due to the high rate of electron capture, but still they can play a major role for the  $\bar{\nu}_e$  spectrum as well (for point (c5), see bottom of fig. 4).

The structure of the  $\beta$  spectra in Figs. 3 and 4 is as expected: one can identify the characteristic smooth shape of  $\beta$  decay spectra and, especially at lower temperatures (e.g., point (c1)), the peaks due to electron capture. At higher temperatures, these peaks are widened by thermal effects (see e.g., [9]) and ultimately form a continuum with one another and with the electron capture spectrum (points (c3), (c4) and (c5)).

We have identified the specific decays that produce the most prominent  $\beta$  peaks. For points (c1) and (s2), with relatively low temperatures and densities, the major contributors are isotopes around  $A \approx 30$ . In particular, the two peaks at high energy in the  $\nu_e$  spectrum for point (c1) are produced by electron capture on  $^{30}\text{P}$  and  $^{31}\text{S}$ . Similarly, the bump in the spectrum around  $E \approx 4 \text{ MeV}$  in the  $\bar{\nu}_e$  spectrum in point (c1) is from positron capture on  $^{32}\text{P}$ . For point (s2), the high energy peak in  $\nu_e$  is due to electron capture on  $^{27}\text{Si}$ . As the temperature and density increases, the isotopes dominating the  $\beta$  process spectrum move to higher  $A$ . The  $\nu_e$  and  $\bar{\nu}_e$  spectra for points (c3) - (c5) have the highest contributions from iron, cobalt, manganese and chromium isotopes. This is consistent with the findings of Odrzywolek [9]. The possibility that these decays might, at least in principle, be observed in a neutrino spectrum could serve as motivation for further theoretical study.

#### IV. SUMMARY AND DISCUSSION

We have performed a new study of the neutrino emission from a presupernova from thermal and beta processes, using

updated nuclear rate tables and modeling the neutrino spectra from each process in detail. The microphysics was then applied to a realistic numerical model of a time-evolving star, using the output of the MESA code. The  $\nu_e$  and  $\bar{\nu}_e$  emissivities and spectra were calculated for selected times and locations inside the star, with particular emphasis on the detectable part of the spectrum, above an indicative threshold of 2 MeV.

It was found that, in part of the parameter space,  $\beta$  processes contribute substantially to the detectable neutrino flux, even when they are subdominant to the entire neutrino emissivity (integrated over the entire spectrum). Some of the  $\beta$  decays that contribute the most, due to having high  $Q$ -value, were identified; they would be an interesting target of further study to obtain more reliable spectra above realistic detection thresholds.

A step forward towards a study of the detectability of presupernova neutrinos will be to integrate the emissivity over the whole star's core and inner shells and for several time steps, so as to obtain the total neutrino flux and its time evolution.

If the presupernova neutrino emission is detectable, it would be interesting to study its dependence on the progenitor star. In contrast with the post-collapse neutrino burst, which is fairly universal in first approximation, strong variations are expected in the presupernova emission depending on the mass and type of progenitor. In particular, the time evolution of the neutrino flux should be strongly progenitor-dependent, reflecting the faster evolution of more massive stars through the different stages of nuclear burning (see e.g., [18]). Therefore, the detection of the presupernova emission might be a new tool to learn about supernova progenitors; this aspect can be investigated with MESA, which can calculate the presupernova evolution over a wide range of progenitor masses.

We find that the  $\nu_e$  and  $\bar{\nu}_e$  fluxes should dominate over the  $\nu_x$  ones. This could, in principle, make presupernova neutrinos a tool to test neutrino oscillations by looking for the permutation of energy spectra of the different flavors. Interestingly, the oscillation pattern might be different from that expected for the post-collapse flux. Specifically, the presupernova flux might be free from the still poorly understood collective oscillation effects – driven by neutrino-neutrino coherent scattering – (see e.g., [41, 42]) that are active when the number flux of neutrinos is high and the matter density profile is suppressed behind the launched shockwave [4, 43]. Without the compli-



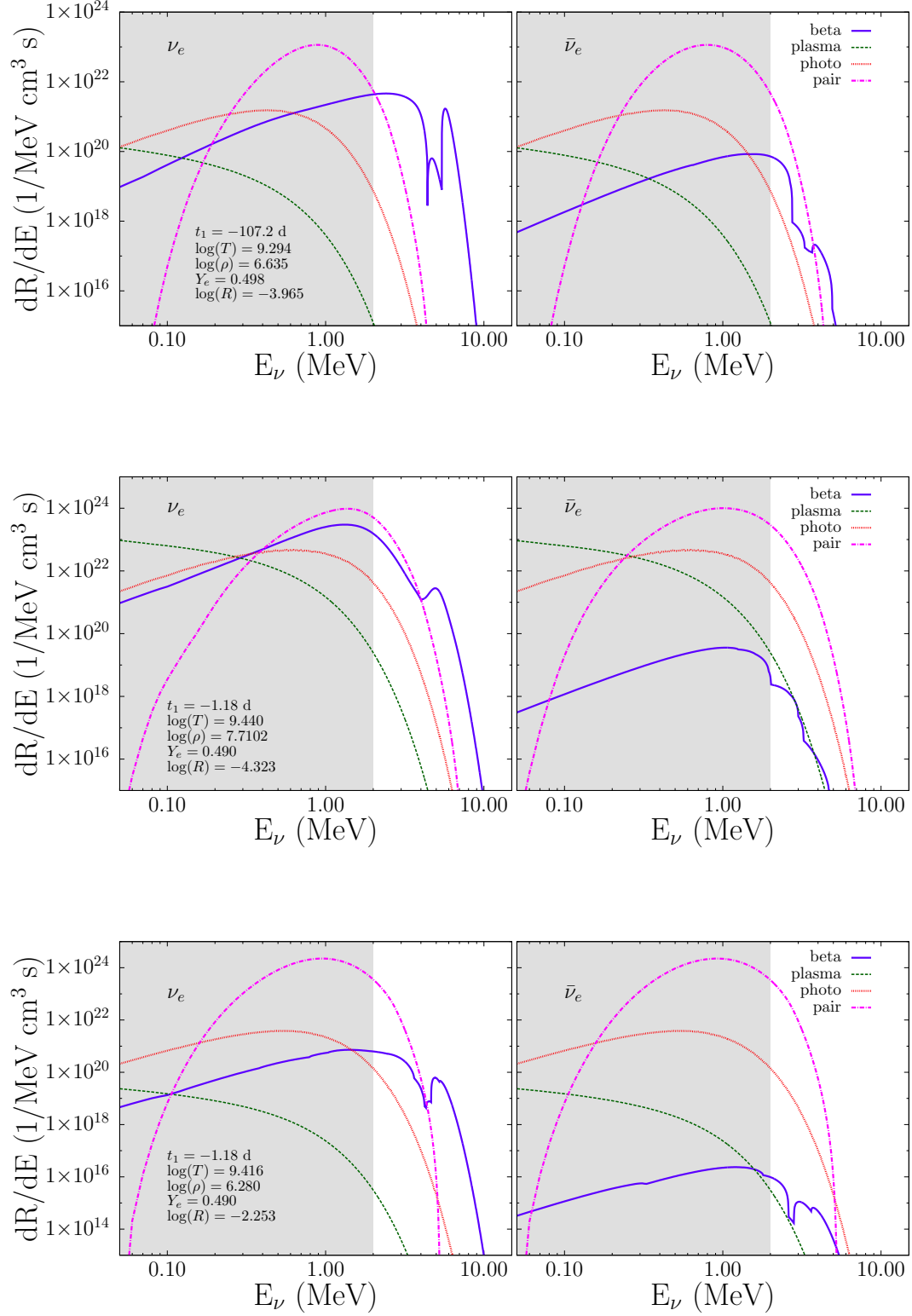


FIG. 3: Neutrino spectra for different processes, for the sample points (c1), (c2) and (s2) in Table II (from top to bottom, in the order they appear in the table), and for  $\nu_e$  (left column) and  $\bar{\nu}_e$  (right column). The detectable part of the spectrum is shown with light background.

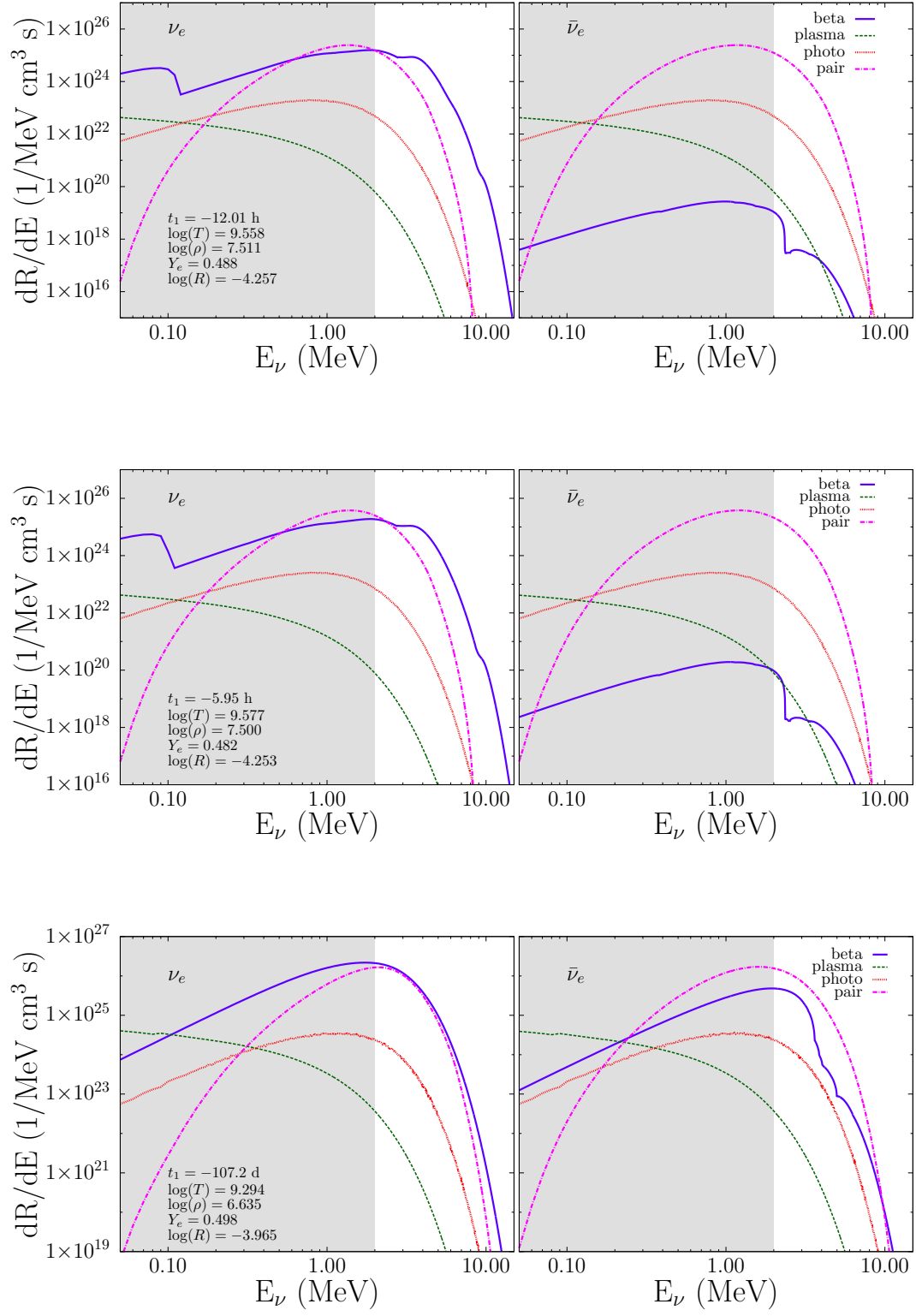


FIG. 4: The same as fig. 3, for the sample points (c3)-(c5) in Table II.

cation of collective effects, oscillations of presupernova neutrinos might offer a particularly clean test of the matter-driven flavor conversion (MSW effect [44–46]).

### Acknowledgments

We are deeply grateful to F. X. Timmes for very insightful comments and encouragement, and thank A. Odrzywolek for fruitful discussion. We also acknowledge the National Science Foundation grant number PHY-1205745.

### Appendix A: Plasma properties

The calculation of the plasma neutrino spectrum in Section II B 1 requires the definition of several properties of the plasma. The plasma frequency is defined as the energy of a plasmon with zero momentum, and is written as [22]:

$$\omega_0 = \frac{4\alpha}{\pi} \int_0^\infty \frac{p^2}{E} \left(1 - \frac{v^2}{3}\right) (f_1 + f_2) dp, \quad (\text{A1})$$

with  $\alpha$  being the fine-structure constant, and  $f_i$  ( $i = 1, 2$ ) the electron and positron distributions:

$$f_1 = \frac{1}{1 + \exp((E - \mu_e)/kT)} \quad (\text{A2})$$

$$f_2 = \frac{1}{1 + \exp((E + \mu_e)/kT)}, \quad (\text{A3})$$

$p = \sqrt{E^2 + m_e^2}$ , and  $v = p/E$ . Here,  $\mu_e$  is the chemical potential, including the electron mass, which depends on the temperature and density of the medium.

The first relativistic correction to the plasma frequency is defined similarly as [22]

$$\omega_1 = \frac{4\alpha}{\pi} \int_0^\infty \frac{p^2}{E} \left(\frac{5}{3}v^2 - v^4\right) (f_1 + f_2) dp. \quad (\text{A4})$$

With  $\omega_0$  and  $\omega_1$ , we can define the typical velocity of electrons in the plasma:  $v_\star = \omega_1/\omega_0$ .

The dispersion relations for the longitudinal and transverse plasmons, in general, are given by [21]:

$$k^2 = \Pi_L(\omega_L(k), k), \quad (\text{A5})$$

$$k^2 = \omega_T^2 - \Pi_T(\omega_T(k), k), \quad (\text{A6})$$

where  $\Pi_L$  and  $\Pi_T$  are the longitudinal and transverse polarization functions, seen earlier in Eqs. (13) and (14). In our calculations, we have used the Braaten-Segel approximations [36], which allow us to write these polarization functions as

$$\Pi_L = 3 \frac{\omega_0^2}{v_\star^2} \left( \frac{\omega_L}{2v_\star k} \log \left[ \frac{\omega_L + v_\star k}{\omega_L - v_\star k} \right] - 1 \right), \quad (\text{A7})$$

$$\Pi_T = \frac{3\omega_0^2}{2v_\star^2} \left( \frac{\omega_T^2}{k^2} - \frac{\omega_T^2 - v_\star^2 k^2}{k^2} \frac{\omega_T}{2v_\star k} \log \left[ \frac{\omega_T + v_\star k}{\omega_T - v_\star k} \right] \right). \quad (\text{A8})$$

With these approximations, the dispersion relations are [22]:

$$k^2 = 3 \frac{\omega_0^2}{v_\star^2} \left( \frac{\omega_L}{2v_\star k} \log \left[ \frac{\omega_L + v_\star k}{\omega_L - v_\star k} \right] - 1 \right) \quad (\text{A9})$$

for the longitudinal plasmons and

$$\omega_T^2 = k^2 + \omega_0^2 \frac{3\omega_T^2}{2v_\star^2 k^2} \left( 1 - \frac{\omega_T^2 - v_\star^2 k^2}{2\omega_T v_\star k} \log \left[ \frac{\omega_T + v_\star k}{\omega_T - v_\star k} \right] \right) \quad (\text{A10})$$

for the transverse plasmons. The energy of the transverse plasmons is not limited ( $\omega_{max} \rightarrow \infty$ ), but longitudinal plasmons must satisfy  $\omega_L < \omega_{max}$  where, in the Braaten-Segel approximation,

$$\omega_{max}^2 = k_{max}^2 = \frac{3\omega_0^2}{2v_\star^2} \left( \frac{1}{2v_\star} \log \left[ \frac{1 + v_\star}{1 - v_\star} \right] - 1 \right). \quad (\text{A11})$$

The final polarization function  $\Pi_A$  from Eq. (14) is given by [22]:

$$\Pi_A = \omega_A k \frac{\omega_T^2 - k^2}{\omega_T^2 - v_\star^2 k^2} \frac{3\omega_0^2 - 2(\omega_T^2 - k^2)}{\omega_0^2} \quad (\text{A12})$$

where  $\omega_A$  is the axial polarization coefficient given by

$$\omega_A = \frac{2\alpha}{\pi} \int_0^\infty \frac{p^2}{E^2} \left( 1 - \frac{2}{3}v^2 \right) (f_1 - f_2) dp. \quad (\text{A13})$$

With reference to the plasmon decay rates and emissivities, Eqs. (10) and (11), the residues  $Z_{L,T}(k)$ , are, in the Braaten-Segel approximation [21]:

$$\begin{aligned} Z_L &= \left( -\frac{\omega_L^2}{k^2} \frac{\partial \Pi_L}{\partial \omega^2} \right)^{-1} = \frac{\omega_L^2}{\omega_L^2 - k^2} \frac{2(\omega_L^2 - v_\star^2 k^2)}{3\omega_0^2 - \omega_L^2 + v_\star^2 k^2}, \quad (\text{A14}) \\ Z_T &= \left( 1 - \frac{\partial \Pi_T}{\partial \omega^2} \right)^{-1} \\ &= \frac{2\omega_T^2 (\omega_T^2 - v_\star^2 k^2)}{3\omega_0^2 \omega_T^2 + (\omega_T^2 + k^2)(\omega_T^2 - v_\star^2 k^2) - 2\omega_T^2 (\omega_T^2 - k^2)}. \end{aligned} \quad (\text{A15})$$

In the differential rate, Eq. (17), the Jacobean resulting from integration with the  $\delta$  function is defined as [22]:

$$J_{L,T} = \frac{\mathcal{E}_1 \mathcal{E}_2}{k} \frac{\partial \omega_{L,T}}{\partial k} \Big|_{k=k'}. \quad (\text{A16})$$

Once again, the Braaten-Segel approximation allows us to write these functions simply as

$$J_L = \left| \frac{k^2}{\mathcal{E}_1 \mathcal{E}_2} \frac{1 - \beta_L}{\omega_L \beta_L} \right|, \quad (\text{A17})$$

$$J_T = \left| \frac{\mathcal{E}_1 + \mathcal{E}_2}{\mathcal{E}_1 \mathcal{E}_2} \frac{1 - \beta_T}{1 - \frac{\omega_T^2}{k^2} \beta_T} \right|, \quad (\text{A18})$$

where the functions  $\beta_{L,T}$  are

$$\beta_L = \frac{3\omega_0^2}{2v_\star^3} \left( \frac{3\omega_L}{2k^3} \log \left[ \frac{\omega_L + v_\star k}{\omega_L - v_\star k} \right] - \frac{\omega_L^2 v_\star}{k^2(\omega_L^2 - v_\star^2 k^2)} - \frac{2v_\star}{k^2} \right), \quad (\text{A19})$$

$$\beta_T = \frac{9\omega_0^2}{4v_\star^2 k^2} \left( 1 + \frac{1}{6} \left( \frac{v_\star k}{\omega_T} - \frac{3\omega_T}{v_\star k} \right) \log \left[ \frac{\omega_T + v_\star k}{\omega_T - v_\star k} \right] \right). \quad (\text{A20})$$

These definitions, when used with the information given in Section II B 1, allows for the calculation of plasma neutrino spectra. More discussion and detailed derivations of these expressions, and the matrix elements in Eqs. (13) and (14) can be found in references [21, 22, 36].

### Appendix B: Photoneutrino process formalism

The matrix element defined in equation (21) includes the terms  $\mathcal{M}_-$ ,  $\mathcal{M}_+$ , and  $\mathcal{M}_\times$ . We refer to Dutta *et al.* [23] for details about them; here we report their expressions as used in our calculation.

It is first necessary to define several simplifying notations [23]:

$$P_t = p + p', \quad (\text{B1})$$

$$\mathcal{B}_- = \frac{1}{\beta_1} - \frac{1}{\beta_2}, \quad (\text{B2})$$

$$\mathcal{B}_+ = \frac{1}{\beta_1} + \frac{1}{\beta_2}, \quad (\text{B3})$$

$$S(x, y, w, z) = (x \cdot w)(y \cdot z) + (x \cdot z)(y \cdot w), \quad (\text{B4})$$

$$R(x, y, w, z) = (x \cdot w)(y \cdot z) - (x \cdot z)(y \cdot w), \quad (\text{B5})$$

$$W(x, y, z) = (x \cdot k)(y \cdot k) - (x \cdot y)k^2 - (x \cdot k)(z \cdot y) \quad (\text{B6})$$

The terms  $\beta_{1,2}$  are defined as

$$\beta_1 = 2p \cdot k + k^2, \quad (\text{B7})$$

$$\beta_2 = -2p' \cdot k + k^2. \quad (\text{B8})$$

Finally, we define the functions  $P^T$  and  $P^L$  as

$$P^T(x, y) = \mathbf{x} \cdot \mathbf{y} - \frac{(\mathbf{x} \cdot \mathbf{k})(\mathbf{y} \cdot \mathbf{k})}{\mathbf{k}^2}, \quad (\text{B9})$$

$$P^L(x, y) = -x \cdot y + \frac{(x \cdot k)(y \cdot k)}{k^2} - P^T(x, y). \quad (\text{B10})$$

With these additional definitions, we can now write the terms  $\mathcal{M}_-$ ,  $\mathcal{M}_+$ , and  $\mathcal{M}_\times$  for the transverse mode:



$$\mathcal{M}_-^T = 2q_1 \cdot q_2 \left[ k^2 \mathcal{B}_-^2 - 2 \left( \frac{P^T(p, p)}{\beta_1^2} + \frac{P^T(p', p')}{\beta_2^2} + \frac{2P^T(p, p')}{\beta_1 \beta_2} \right) \right] + 4 \left[ \frac{2k \cdot q_1 k \cdot q_2 - k^2 P^T(q_1 q_2)}{\beta_1 \beta_2} \right], \quad (\text{B11})$$

$$\begin{aligned} \mathcal{M}_+^T = & 2S(p, p', q_1, q_2) \left[ -k^2 \mathcal{B}_+^2 + 2 \left( \frac{P^T(p, p)}{\beta_1^2} + \frac{P^T(p', p')}{\beta_2^2} + \frac{2P^T(p, p')}{\beta_1 \beta_2} \right) \right] \\ & + 4S(k, p', q_1, q_2) \left[ \frac{k \cdot p}{\beta_1} \mathcal{B}_+ + \frac{1}{\beta_1} \left( \frac{P^T(p, p)}{\beta_1} + \frac{P^T(p, p')}{\beta_2} \right) \right] + 4S(k, p, q_1, q_2) \left[ \frac{k \cdot p'}{\beta_2} \mathcal{B}_+ - \frac{1}{\beta_2} \left( \frac{P^T(p, p')}{\beta_1} + \frac{P^T(p', p')}{\beta_2} \right) \right] \\ & + \frac{4}{\beta_1 \beta_2} \left[ P^T(p', q_2) W(p, q_1, P_t) + P^T(p', q_1) W(p, q_2, P_t) + P^T(p, q_2) W(p', q_1, -P_t) + P^T(p, q_1) W(p', q_2, -P_t) \right. \\ & - P^T(p, p') (2k \cdot q_1 k \cdot q_2 - k^2 q_1 \cdot q_2) + P^T(q_1, q_2) (k^2 p \cdot p' - 2p \cdot k p' \cdot k) \\ & \left. + 2q_1 \cdot q_2 (k^2 p \cdot p' - p \cdot k p' \cdot k) - 2p \cdot p' k \cdot q_1 k \cdot q_2 \right], \end{aligned} \quad (\text{B12})$$

$$\begin{aligned} \mathcal{M}_\times^T = & \frac{2}{\beta_1^2} \left\{ \left[ -2k^2 + 4P^T(p, p) \right] R(p', p, q_1, q_2) + 2\beta_1 \left[ p' \cdot q_2 P^T(p, q_1) - p' \cdot q_1 P^T(p, q_2) \right] + \left[ 4p \cdot k + 4P^T(p, p) \right] R(p', k, q_1, q_2) \right\} \\ & + \frac{2}{\beta_2^2} \left\{ \left[ -2k^2 + 4P^T(p', p') \right] R(p', p, q_1, q_2) - 2\beta_2 \left[ p \cdot q_2 P^T(p', q_1) - p \cdot q_1 P^T(p', q_2) \right] - \left[ 4p' \cdot k - 4P^T(p', p') \right] R(p, k, q_1, q_2) \right\} \\ & + \frac{4}{\beta_1 \beta_2} \left\{ 2P^T(p, p') \left[ R(p', k, q_1, q_2) + 2R(p', p, q_1, q_2) + R(p, k, q_1, q_2) \right] \right. \\ & 2 \left[ k \cdot p' R(p, k, q_1, q_2) + k^2 R(p', p, q_1, q_2) - p \cdot k R(p', k, q_1, q_2) \right] \\ & + P^T(p, q) \left( 2p' \cdot k k \cdot q_2 + 2k \cdot p' p \cdot q_2 - p' \cdot q_2 k^2 \right) - P^T(p, q_2) \left( 2p' \cdot k k \cdot q_1 + 2k \cdot p' p \cdot q_1 - p' \cdot q_1 k^2 \right) \\ & \left. + P^T(p', q_2) \left( 2p \cdot k k \cdot q_1 - 2p' \cdot q_1 p \cdot k - p \cdot q_1 k^2 \right) - P^T(p', q_1) \left( 2p \cdot k k \cdot q_2 - 2p \cdot k p' \cdot q_2 - p \cdot q_2 k^2 \right) \right\}. \end{aligned} \quad (\text{B13})$$

---

For the longitudinal mode, the expressions are similar [23]:

---

$$\mathcal{M}_-^L = q_1 \cdot q_2 \left[ k^2 \mathcal{B}_-^2 - 4 \left( \frac{P^L(p, p)}{\beta_1^2} + \frac{P^L(p', p')}{\beta_2^2} + \frac{2P^L(p, p')}{\beta_1 \beta_2} \right) \right] + 4 \left[ \frac{2k \cdot q_1 k \cdot q_2 - k^2 P^L(q_1 q_2)}{\beta_1 \beta_2} \right], \quad (\text{B14})$$

$$\begin{aligned} \mathcal{M}_+^L = & 2S(p, p', q_1, q_2) \left[ -k^2 \mathcal{B}_+^2 + 4 \left( \frac{P^L(p, p)}{\beta_1^2} + \frac{P^L(p', p')}{\beta_2^2} + \frac{2P^L(p, p')}{\beta_1 \beta_2} \right) \right] \\ & + 2S(k, p', q_1, q_2) \left[ \frac{k \cdot p}{\beta_1} \mathcal{B}_+ + \frac{2}{\beta_1} \left( \frac{P^L(p, p)}{\beta_1} + \frac{P^L(p, p')}{\beta_2} \right) \right] + 2S(k, p, q_1, q_2) \left[ \frac{k \cdot p'}{\beta_2} \mathcal{B}_+ - \frac{2}{\beta_2} \left( \frac{P^L(p, p')}{\beta_1} + \frac{P^L(p', p')}{\beta_2} \right) \right] \\ & + \frac{4}{\beta_1 \beta_2} \left[ P^L(p', q_2) W(p, q_1, P_t) + P^L(p', q_1) W(p, q_2, P_t) + P^L(p, q_2) W(p', q_1, -P_t) + P^L(p, q_1) W(p', q_2, -P_t) \right. \\ & - P^L(p, p') (2k \cdot q_1 k \cdot q_2 - k^2 q_1 \cdot q_2) + P^L(q_1, q_2) (k^2 p \cdot p' - 2p \cdot k p' \cdot k) \\ & \left. + q_1 \cdot q_2 (k^2 p \cdot p' - p \cdot k p' \cdot k) - p \cdot p' k \cdot q_1 k \cdot q_2 \right], \end{aligned} \quad (\text{B15})$$

$$\begin{aligned} \mathcal{M}_\times^L = & \frac{2}{\beta_1^2} \left\{ \left[ -k^2 + 4P^L(p, p) \right] R(p', p, q_1, q_2) + 2\beta_1 \left[ p' \cdot q_2 P^L(p, q_1) - p' \cdot q_1 P^L(p, q_2) \right] + \left[ 2p \cdot k + 4P^L(p, p) \right] R(p', k, q_1, q_2) \right\} \\ & + \frac{2}{\beta_2^2} \left\{ \left[ -k^2 + 4P^L(p', p') \right] R(p', p, q_1, q_2) - 2\beta_2 \left[ p \cdot q_2 P^L(p', q_1) - p \cdot q_1 P^L(p', q_2) \right] - \left[ 2p' \cdot k - 4P^L(p', p') \right] R(p, k, q_1, q_2) \right\} \\ & + \frac{4}{\beta_1 \beta_2} \left\{ 2P^L(p, p') \left[ R(p', k, q_1, q_2) + 2R(p', p, q_1, q_2) + R(p, k, q_1, q_2) \right] \right. \\ & \left[ k \cdot p' R(p, k, q_1, q_2) + k^2 R(p', p, q_1, q_2) - p \cdot k R(p', k, q_1, q_2) \right] \\ & + P^L(p, q) \left( 2p' \cdot k k \cdot q_2 + 2k \cdot p' p \cdot q_2 - p' \cdot q_2 k^2 \right) - P^L(p, q_2) \left( 2p' \cdot k k \cdot q_1 + 2k \cdot p' p \cdot q_1 - p' \cdot q_1 k^2 \right) \\ & \left. + P^L(p', q_2) \left( 2p \cdot k k \cdot q_1 - 2p' \cdot q_1 p \cdot k - p \cdot q_1 k^2 \right) - P^L(p', q_1) \left( 2p \cdot k k \cdot q_2 - 2p \cdot k p' \cdot q_2 - p \cdot q_2 k^2 \right) \right\}. \end{aligned} \quad (\text{B16})$$

As with the plasma neutrino process, we must define the dispersion relations for both the transverse and longitudinal photons. In this case, we can use a simple first order approximation, where

$$\omega_T^2 = \omega_0^2 + |\mathbf{k}|^2, \quad (\text{B17})$$

$$\omega_L^2 = \omega_0^2, \quad (\text{B18})$$

with  $\omega_0$  being the plasma frequency, eq. (A1). From these expressions, we find

$$m_k^T = \omega_0, \quad (\text{B19})$$

$$m_k^L = \sqrt{\omega_0^2 - |\mathbf{k}|^2}. \quad (\text{B20})$$

These definitions are needed to find the value of the photon angle  $\theta_k$  given in equation (22).

Also needed for the integration are the minimum and maximum allowed photon momenta. The values differ between the transverse and longitudinal modes. In the case of the trans-

verse mode, the values are found to be [23]

$$|\mathbf{k}|^\pm = \left[ \left( \frac{EA \pm |\mathbf{P}| \sqrt{A^2 - 4M^2\omega_0^2}}{2M^2} \right)^2 - \omega_0^2 \right]^{1/2}, \quad (\text{B21})$$

and for longitudinal photons:

$$|\mathbf{k}|^\pm = \left[ (2|\mathbf{P}|^2 - 2\omega_0 E + A) \pm \sqrt{(2|\mathbf{P}|^2 - 2\omega_0 E + A)^2 - (4\omega_0^2 E^2 - 4\omega_0 EA + A^2)} \right]^{1/2}. \quad (\text{B22})$$

with  $A = M^2 + \omega_0^2 - m_e^2$ .

With these definitions, all of the necessary information for the calculation of the photoneutrino spectrum discussed in Section II B 2 is available. More discussion and a full derivation of these expressions can be found in [23].

- 
- [1] K. Hirata *et al.*, Phys. Rev. Lett. **58**, 1490 (1987).
  - [2] R. M. Bionta *et al.*, Phys. Rev. Lett. **58**, 1494 (1987).
  - [3] E. N. Alekseev, L. N. Alekseeva, V. I. Volchenko, and I. V. Krivosheina, J. Exptl. Theoret. Phys. Lett. **45**, 589 (1987).
  - [4] A. Mirizzi, I. Tamborra, H.-T. Janka, N. Saviano, K. Scholberg, R. Bollig, L. Hudepohl, and S. Chakraborty, (2015), arXiv:1508.00785 [astro-ph.HE].
  - [5] A. Odrzywolek and A. Heger, Acta Physica Polonica **B 41**, 1611 (2010).
  - [6] S. E. Woosley, A. Heger, and T. A. Weaver, Rev. Mod. Phys. **74**, 1015 (2002).
  - [7] A. Odrzywolek, M. Misiasek, and M. Kutschera, Astropart. Phys. **21**, 303 (2004), arXiv:astro-ph/0311012.
  - [8] A. Odrzywolek, M. Misiasek, and M. Kutschera, Acta Physica Polonica B **35**, 1981 (2004), arXiv:astro-ph/0405006v1.
  - [9] A. Odrzywolek, Phys. Rev. C **80**, 045801 (2009), arXiv:0903.2311.
  - [10] C. Kato, M. D. Azari, S. Yamada, K. Takahashi, H. Umeda, T. Yoshida, and K. Ishidoshiro, Astrophys. J. (2015), arXiv:1506.02358.
  - [11] K. Asakura *et al.* (KamLAND Collaboration), Preprint (2015), arXiv:1506.01175.
  - [12] K. Langanke and G. Martinez-Pinedo, Atomic Data and Nuclear Data Tables **79**, 1 (2001).
  - [13] T. Oda, M. Hino, K. Muto, M. Takahara, and K. Sato, Atomic Data and Nuclear Data Tables **56**, 231 (1994).
  - [14] G. M. Fuller, W. A. Fowler, and M. J. Newman, Astrophys. J. Suppl. **42**, 447 (1980).
  - [15] G. M. Fuller, W. A. Fowler, and M. J. Newman, Astrophys. J. Suppl. **48**, 279 (1982).
  - [16] G. M. Fuller, W. A. Fowler, and M. J. Newman, Astrophys. J. **252**, 715 (1982).
  - [17] G. M. Fuller, W. A. Fowler, and M. J. Newman, Astrophys. J. **293**, 1 (1985).
  - [18] B. Paxton, L. Bildsten, A. Dotter, F. Herwig, P. Lesaffre, and F. Timmes, Astrophys. J. Suppl. **192**, 3 (2011), arXiv:1009.1622.
  - [19] B. Paxton, M. Cantiello, P. Arras, L. Bildsten, E. F. Brown, A. Dotter, C. Mankovich, M. H. Montgomery, D. Stello, F. X. Timmes, and R. Townsend, Astrophysical Journal Supplemental Series **208**, UNSP 4 (2013), arXiv:1301.0319v2.
  - [20] B. Paxton, P. Marchant, J. Schwab, E. B. Bauer, L. Bildsten, M. Cantiello, L. Dessart, R. Farmer, H. Hu, N. Langer, R. H. D. Townsend, D. M. Townsley, and F. X. Timmes, Preprint (2015), arXiv:1506.03146.
  - [21] S. Ratkovic, S. I. Dutta, and M. Prakash, Phys. Rev. D **67**, 123002 (2003).
  - [22] A. Odrzywolek, Eur. Phys. J. C **52**, 425 (2007).
  - [23] S. I. Dutta, S. Ratkovic, and M. Prakash, Phys. Rev. D **69**, 023005 (2004).
  - [24] M. Misiasek, A. Odrzywolek, and M. Kutschera, Phys. Rev. D **74**, 043006 (2006).
  - [25] K. Langanke, G. Martinez-Pinedo, and J. M. Sampaio, Phys. Rev. C **64**, 055801 (2001).
  - [26] C. Sullivan, E. O'Connor, R. G. T. Zeger, T. Grubb, and S. M. Austin, Preprint (2015), arXiv:1508.07348.
  - [27] A. Heger, S. E. Woosley, G. Martinez-Pinedo, and K. Langanke, Astrophys. J. **560**, 307 (2001).
  - [28] G. Martinez-Pinedo, K. Langanke, and D. J. Dean, ArXiv:nucl-th/9811095.
  - [29] M. B. Aufderheide, I. Fushiki, S. E. Woosley, and D. H. Hartmann, Astrophys. J. Suppl. **91**, 389 (1994).
  - [30] M. B. Aufderheide, I. Fushiki, G. M. Fuller, and T. A. Weaver, Astrophys. J. **424**, 257 (1994).
  - [31] N. Itoh and Y. Kohyama, Astrophys. J. **275**, 858 (1983).
  - [32] N. Itoh, T. Adachi, M. Nakagawa, Y. Kohyama, and H. Munakata, Astrophys. J. **339**, 354 (1989).
  - [33] N. Itoh, H. Mutoh, A. Hikita, and Y. Kohyama, Astrophysical Journal **395**, 622 (1992).
  - [34] N. Itoh, H. Hayashi, A. Nishikawa, and Y. Kohyama, Astrophysical Journal Supplemental Series **102**, 411 (1996).
  - [35] N. Itoh, A. Nishikawa, and Y. Kohyama, Astrophysical Journal **470**, 1015 (1996).
  - [36] E. Braaten and D. Segel, Phys. Rev. D **48**, 1478 (1993).
  - [37] S. Hannestad and J. Madsen, Phys. Rev. D **52**, 1762 (1994).
  - [38] F. An *et al.* (JUNO), (2015),

- arXiv:1507.05613 [physics.ins-det] .
- [39] M. Bishai et al., “Long-Baseline Neutrino Facility (LBNF) and Deep Underground Neutrino Experiment (DUNE) Conceptual Design Report, Vol. 1,” (2015), Available at <http://lbne2-docdb.fnal.gov/cgi-bin/ShowDocument?docid=10687>.
  - [40] K. Abe et al., (2011), arXiv:1109.3262 [hep-ex] .
  - [41] H. Duan and J. P. Kneller, J. Phys. **G36**, 113201 (2009), arXiv:0904.0974 [astro-ph.HE] .
  - [42] H. Duan, G. M. Fuller, and Y.-Z. Qian, Ann. Rev. Nucl. Part. Sci. **60**, 569 (2010), arXiv:1001.2799 [hep-ph] .
  - [43] S. Hannestad, G. G. Raffelt, G. Sigl, and Y. Y. Y. Wong, Phys. Rev. **D74**, 105010 (2006), [Erratum: Phys. Rev.D76,029901(2007)], arXiv:astro-ph/0608695 [astro-ph] .
  - [44] L. Wolfenstein, Phys. Rev. **D17**, 2369 (1978).
  - [45] S. P. Mikheev and A. Yu. Smirnov, Nuovo Cim. **C9**, 17 (1986).
  - [46] S. P. Mikheev and A. Yu. Smirnov, Sov. Phys. JETP **64**, 4 (1986), [Zh. Eksp. Teor. Fiz.91,7(1986)], arXiv:0706.0454 [hep-ph] .